ACS PHYSICAL CHEMISTRY Au
AN OPEN ACCESS JOURNAL OF THE AMERICAN CHEMICAL SOCIETY

pubs.acs.org/physchemau Article

Electronic Structures and Spectroscopic Signatures of Noble-Gas-Doped Nanodiamonds

Ryan A. Beck,[‖] Yue Huang,[‖] Alessio Petrone, Joseph W. Abbott, Peter J. Pauzauskie, and Xiaosong Li*

Cite This: *ACS Phys. Chem Au* 2023, 3, 299–310 Read Online

ACCESS | Metrics & More | Article Recommendations | Supporting Information

ABSTRACT: Fluorescent nanodiamonds, that is, those containing optically active defects, have attracted interest for their ability to be used as qubits; for *in vivo* imaging; and as sensors for spin, stress, and temperature. One of the most commonly studied nanodiamond color centers is the nitrogen vacancy. However, there is strong interest in discovering other impurity centers that provide localized midband gap transitions. Noble gas atoms have garnered attention since they have been discovered within nanodiamonds produced through high-pressure–high-temperature laser-heated diamond anvil cell synthesis methods, where they are commonly used as hydrostatic pressure media. Noble gas atoms that exist in macrosized natural or synthetic diamonds have been shown to be able to form color centers. This research uses *ab initio* density functional theory and cluster models to systematically study the localized electronic structure for group VIII impurities of nanodiamond, including helium, neon, argon, krypton, and xenon. An in-depth examination of the interaction between the noble gas atom and diamond lattice has been carried out. The changes to the vibrational and UV/vis absorption spectra have been analyzed. It was determined that the energetically preferred geometry is dependent on the atom size. Most noble gas defects are stabilized within the nanodiamond lattice and exist in tetrahedral interstitial positions, except for the largest noble gas studied in this work, Xe, which was determined to prefer a substitutional configuration. Both Kr and Xe are expected to be able to manifest visible/near-IR optical responses when included in the diamond lattice.

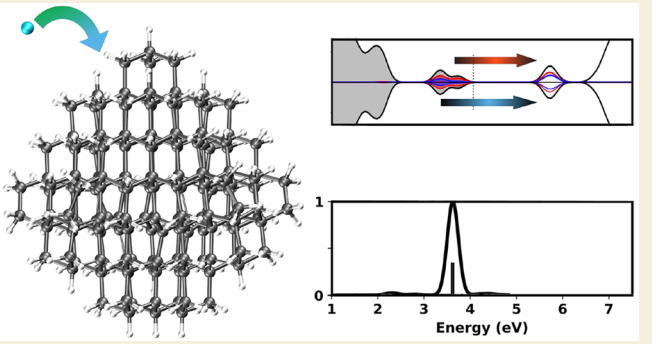

KEYWORDS: *noble gas, defect, nanodiamond, Raman, UV/vis, absorption*

1. INTRODUCTION

Nanodiamonds have been the subject of intense study since the late 1990s for their potential in several applications. Their biocompatibility and ability to carry therapeutics make them excellent candidates for drug delivery,[1] while their superior mechanical, thermal, and surface properties make them ideal materials for nanocomposite.[2,3] Among the different types of nanodiamond, those which contain impurities in the diamond lattice are the most intriguing. They have the potential to form midband gap transition states arising from the presence of dopants within the diamond lattice. These so-called fluorescent nanodiamonds have potential applications for *in vivo* imaging and quantum computing because of their optical and spin properties.[4−7] There is also demand for sensing and cryptography applications because of the high sensitivity of the intraband transitions to small changes in stress and temperature.[4,5,8−12]

There are more than 500 known defects that are optically active in diamond, most are due to the presence of impurity atoms within the diamond.[13] Among them, the most common and studied nanodiamond color center is the nitrogen vacancy (NV) center.[4,5,8,9,14−17] However, negatively charged silicon vacancy (SiV^-) centers have started to attract more attention because of their short fluorescence lifetime and narrow zero-phonon line (ZPL) emission in the infrared range (1.68 eV).[12,18,19] Noble gas defects are another impurity in diamond and have been reported in geological studies to be found in natural diamond,[20,21] in interstellar diamonds located in meteorites (sometimes referred as presolar diamonds),[22−24] and in diamonds doped through ion implantation, wherein a noble gas is commonly used as an inert environment/pressure medium.[25,26]

Even though commonly believed to be inert impurities in a diamond lattice, the noble gas atoms have been shown to form covalently bound defects with surrounding carbon atoms to form color centers.[13,27] Group VIII atoms, helium (He), neon (Ne), argon (Ar), and xenon (Xe), have also been intentionally

Received: December 5, 2022
Revised: January 30, 2023
Accepted: January 31, 2023
Published: February 10, 2023

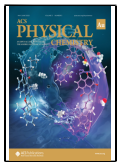

https://doi.org/10.1021/acsphyschemau.2c00072
ACS Phys. Chem Au 2023, 3, 299–310

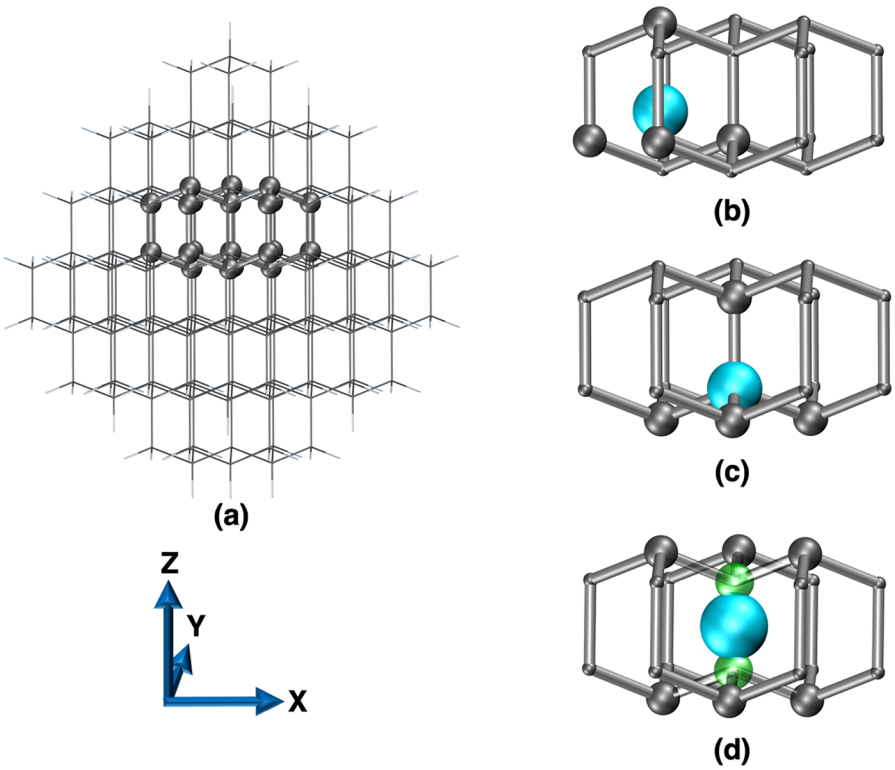

Figure 1. Defect geometries considered in this study. Spheres in gray are carbon atoms, spheres in blue are the dopant atom, and spheres in green mark vacancies. (a) Pure diamond lattice (in wireframe) with the doping site emphasized. The ⟨111⟩ crystallographic axis is parallel to the *Z* Cartesian axis. (b) Interstitial (X_i) dopant in diamond lattice, with the closest four carbon atoms shown with gray spheres. (c) Substitutional (X_s) dopant in place of a carbon atom in the diamond lattice, and the closest four carbon atoms are shown with gray spheres. (d) Split vacancy (X_iV): two adjacent atoms along ⟨111⟩ are removed, and a dopant atom is placed in the central/interstitial position of two vacancies. The closest six carbon atoms are shown with gray spheres.

introduced into diamond, which results in color center formation.[13] For example, He forms thermodynamically stable color centers, in spite of its small atomic size, with visible light range emissions around 580 nm.[28,29] Among the noble gas impurities, Xe has attracted more attention as an impurity in diamond because it can couple with the vacancy in diamond and form stable defects that generate a near-infrared (IR) response at ∼1.53 eV (810 nm).[30,31] The Xe color center is believed to have local D_{3d} symmetry, where the Xe atom occupies the center of a split divacancy in diamond.[13,30−33]

The success of embedding noble gas using ion implantation is limited by the energy of the ion beam and size of the nanodiamond.[34] Between 2001 and 2008, ionized noble gases, including He, Ar, Kr, and Xe, were successfully implanted into synthetic nanodiamonds to compare synthesized nanodiamond to presolar nanodiamond.[24,35] The significance of understanding noble gas defects in nanodiamond increases as more nanodiamond synthetic methods are developed. For example, since noble gases are conventionally treated as chemically inert elements, they also are commonly used as near-hydrostatic pressure media in the high-pressure−high-temperature (HPHT) synthesis of nanodiamond.[10] Such conditions provide the potential for these dopants to be incorporated into the synthesized nanodiamond lattice as interstitial or substitutional defects. Recently, nanodiamonds synthesized through HPHT were confirmed to have incorporated Ar.[12] However, it is unknown if this incorporated Ar is able to introduce color centers to the nanodiamond system. Thus, a systematic study of noble gas defects in nanodiamonds is needed to help identify these centers and provide insight into their spectroscopic signatures.

Despite the significance of noble gas impurities in diamond and the evidence of noble gas defects in presolar nanodiamond,[24] there are limited theoretical studies focusing on the electronic structure and the UV/vis absorption spectra of noble-gas-doped nanodiamonds. These are needed to identify the various geometric configurations and explain why a near-infrared ZPL can be found in Xe-defected diamond but not in other noble gas diamonds. In this work, different geometric configurations of the group VIII atom nanodiamond impurities, including He, Ne, Ar, Kr, and Xe, are studied. The stability between the configurations is determined, and the vibrational Raman and UV/vis absorption spectroscopic signatures of each geometry are calculated.

2. METHODOLOGY

In this study, nearly spherical diamond quantum dots ($C_{182}H_{142}$) were constructed using the 0.357 nm lattice parameter of bulk face-centered cubic diamond,[36] thereby forming nanodiamond clusters with a diameter of ∼1.4 nm. This is smaller than, though approaching, experimental size.[10,37−39] The dangling bonds on the surface of the diamond were passivated by hydrogen atoms according to the procedure described in ref 16. To construct the defect-containing nanodiamond, a noble gas atom (He, Ne, Ar, Kr, or Xe) is embedded into the nanodiamond lattice, which results in a nonsurface defect. These models have been previously shown to be effective in studying both the electronic and vibrational

https://doi.org/10.1021/acsphyschemau.2c00072
ACS Phys. Chem Au 2023, 3, 299−310

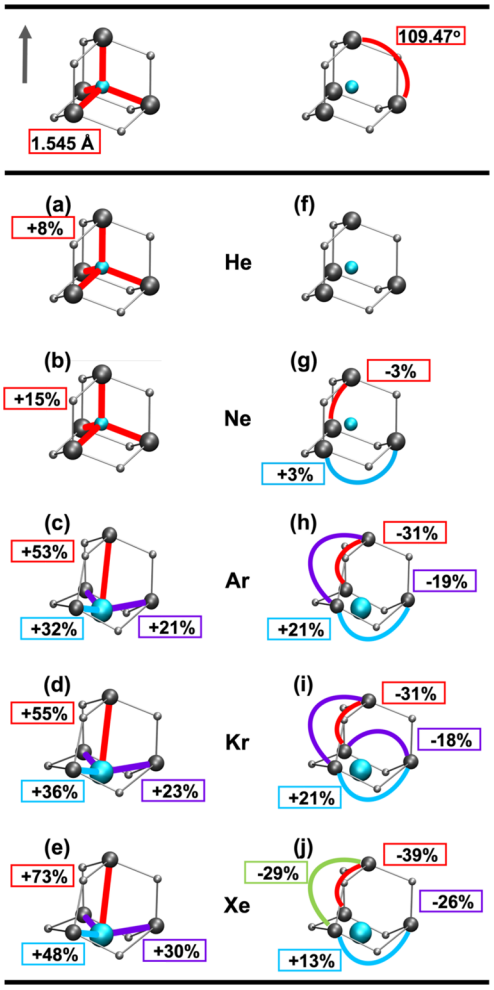

Figure 2. Geometric structural changes after optimization of He, Ne, Ar, Kr, and Xe's interstitial configuration; blue shows the noble gas dopant, and gray shows the nearest carbon atoms, as highlighted in Figure 1. The top panel shows the bond length and bond angle, respectively, before relaxation. (a–e) Change of bond length and (f–j) change of bond angle. The gray arrow lays along the crystallographic ⟨111⟩ axis. Identical distortions are marked with the same color.

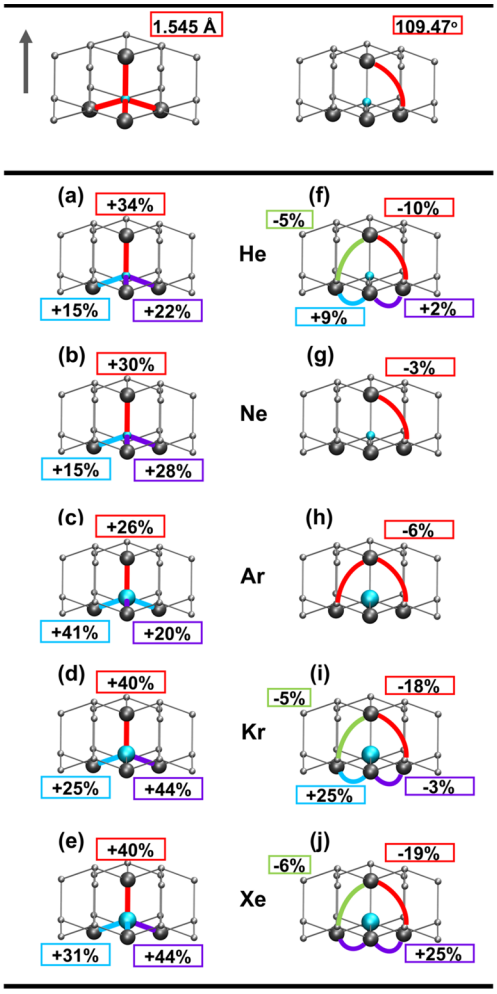

Figure 3. Geometric structural changes after optimization of He, Ne, Ar, Kr, and Xe's substitutional configuration; blue shows the noble gas dopant, and gray shows the nearest carbon atoms, as highlighted in Figure 1. The top panel shows the bond length and bond angle, respectively, before relaxation. (a–e) The change of bond length and (f–j) change of bond angle. The gray arrow lays along the crystallographic ⟨111⟩ axis. Identical distortions are marked with the same color.

responses of pure and doped nanodiamond systems containing nitrogen and silicon vacancies,[12,16−18] as well as surface defects.[40] Since the diamond Bohr exciton radius is ∼1.6 nm,[41] the systems in this work are expected to exhibit quantum confinement effects.

All calculations were carried out using the Gaussian 16 electronic structure software package.[42] The Kohn−Sham equation is solved using the hybrid Becke, 3-parameter, Lee−Yang−Parr (B3LYP) density functional to obtain the ground-state electronic structures,[43−45] with a 6-31G(d) basis set for the carbon and hydrogen atoms. To account for scalar relativistic effects in the heavier atoms, the Stuttgart relativistic pseudopotential and associated basis sets[46−71] were used for all noble gases except He and Ne, which used a 6-31G(d) basis. Geometries were considered optimized when the maximum and root-mean-square (RMS) forces were less than 0.000450 and 0.000300 hartree/Bohr, respectively, and maximum and RMS displacements were less than 0.0018 and 0.0012 Bohr, respectively. Time-dependent density functional theory (TDDFT) within the linear response framework[72−75] was used to calculate the electronic structure of the excited states.

3. RESULTS AND DISCUSSION

3.1. Defect Structures

There are two categories of point defects that involve implanting a dopant into a nanodiamond, interstitial point defects (X_i) and substitutional point defects (X_s). For each category there are several different possible ways to construct the geometry of the system. Three possible geometries are used in this work, which are exhibited in Figure 1 alongside a perfect spherical nanodiamond (Figure 1a). For the interstitial point defect, the most probable location is at the highest symmetry interstitial space inside the diamond lattice at the center of one of the tetrahedrons. Since only one interstitial system is studied in this research, this system is labeled X_i, (Figure 2b). For the substitutional (X_s) defect, shown in Figure 1c, one of the carbon atoms is removed and replaced with a noble gas dopant. This leads to a local T_d symmetry

https://doi.org/10.1021/acsphyschemau.2c00072
ACS Phys. Chem Au 2023, 3, 299−310

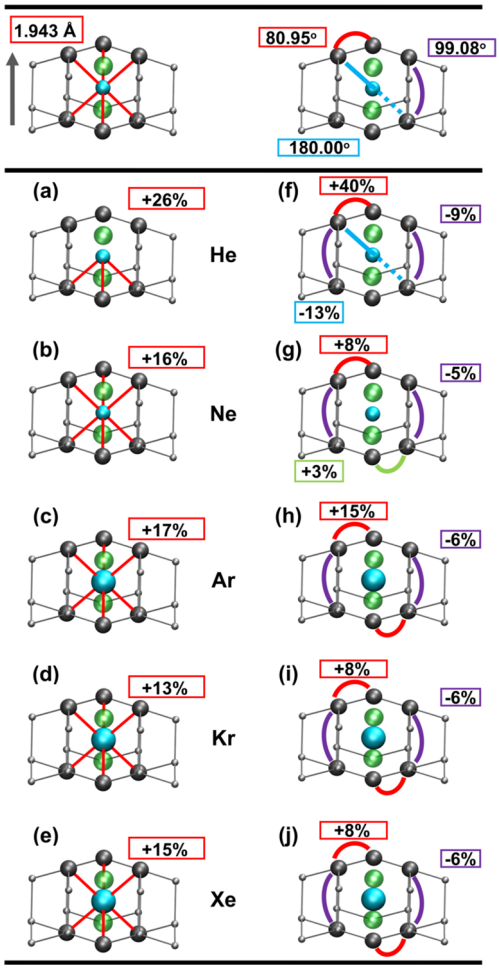

Figure 4. Geometric structural changes after optimization of He, Ne, Ar, Kr, and Xe's split-vacancy configuration. Blue spheres show the noble gas dopant, green spheres show vacant positions, and gray spheres show the nearest carbon atoms, as highlighted in Figure 1. The top panel shows the bond length and bond angle, respectively, before relaxation. (a–e) The change of bond length and (f–j) change of bond angle. The gray arrow lays along the crystallographic ⟨111⟩ axis. Identical distortions are marked with the same color.

Table 1. Formation Enthalpies of the Tested Geometric Configurations of the Noble-Gas-Doped Nanodiamond Systems[a]

dopant atom	geometry	formation enthalpy (eV)
He	**X_i**	**6.22**
	X_s	18.58
	X_iV	30.30
Ne	**X_i**	**18.06**
	X_s	23.90
	X_iV	32.93
Ar	**X_i**	**27.85**
	X_s	31.20
	X_iV	36.64
Kr	**X_i**	**31.07**
	X_s	32.37
	X_iV	37.69
Xe	X_i	36.25
	X_s	**35.99**
	X_iV	39.19

[a]The most stable geometry for each system is shown in bold.

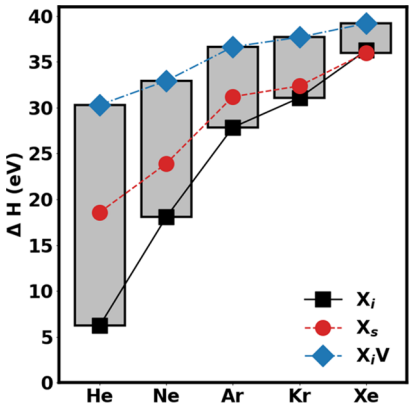

Figure 5. Enthalpy of formation for the defects reported in Table 1. Each noble gas species has their three structures marked, with the range between the highest and lowest enthalpies shown with a gray rectangle. It can be observed that as the size of the noble gas increases, the energy to form the defects increases, while the difference in energy between each formed defect decreases.

within the C_{3v} symmetry of the entire cluster. The split vacancy (X_iV, Figure 1d) geometry is formed when a dopant takes the center position between two adjacent carbon vacancies along the ⟨111⟩ crystallographic axis, thereby resulting in a local D_{3d} symmetry. This is the same geometry that has been seen for other diamond defects, such as SiV.[18,76]

All configurations shown in Figure 1 are constructed and have their geometries optimized for each noble-gas-doped nanodiamond system. The results of the geometry relaxations are given in Figures 2–4.

Figure 2 presents the geometric reorganization of the He, Ne, Ar, Kr, and Xe-doped nanodiamonds in the interstitial doping structure, X_i, compared to the pure diamond crystal lattice. Before geometry reorganization, the noble gas atom is located at the center of a symmetrical tetrahedron of the fcc structure. The distance from the noble gas to the nearest carbon R_{XC} = 1.544 Å, and the angle $\angle_{CXC}$ = 109.5°. Figure 2 shows that the 3-fold symmetry along the ⟨111⟩ direction and local T_d symmetry is mostly kept after relaxations both for He and Ne interstitial doping structures. Even though the expansion of the tetrahedron formed by the surrounding four carbons increases with the size of the doped atom, the doped atom is still located at the center of structure and has a similar distance to all surrounding carbons. However, for Ar, Kr, and Xe, not only is the 3-fold symmetry not kept in the ⟨111⟩ direction, but the doped noble gas moves along the ⟨111⟩ axis from the center of the tetrahedron. This results in a heavily distorted local geometry.

The initial local geometry for the substitutional X_s systems is tetrahedral. Figure 3 shows that because of a larger repulsion, the lattice expansion around the noble gas dopant in the substitutional doping position is much greater than in the interstitial structure. The tetrahedral structure is already distorted for the smallest dopant, He, and the distortion increases as the dopant size increases. The strong repulsion between dopant and neighboring carbon atoms eventually leads to a relaxation toward local D_{2d} symmetry.

Figure 4 shows the optimized split-vacancy defect structures. Initial X_iV systems have an R_{XC} bond length of 1.943 Å. Unlike in the tetrahedral systems, there are three unique angles. The first $\angle_{CXC}$ = 80.95° is between two carbons at the same

https://doi.org/10.1021/acsphyschemau.2c00072
ACS Phys. Chem Au 2023, 3, 299–310

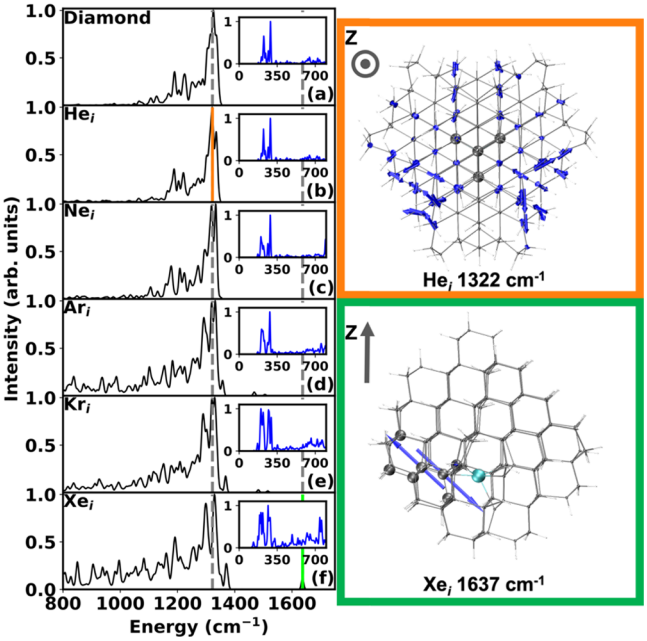

Figure 6. On the left are Raman vibrational spectra for the pure diamond (a) and (b–f) are the X_i-defect-containing diamond systems He, Ne, Ar, Kr, and Xe, respectively. From 800 to 1800 cm^{-1} are the spectra with artificially massed hydrogen to shift the hydrogen–carbon modes away from the carbon–carbon stretching modes. Inset into each plot are the Raman absorption spectra with regular massed hydrogen to show the low-energy responses. On the right are select normal modes with the noble gas in cyan, select carbon atoms in gray, the diamond lattice in wireframe, and the normal mode displacement vectors in dark blue. In gray is shown the orientation of the Cartesian Z axis, which aligns with the crystallographic ⟨111⟩ axis. Spectral locations of the select normal modes are color-labeled on the Raman spectra.

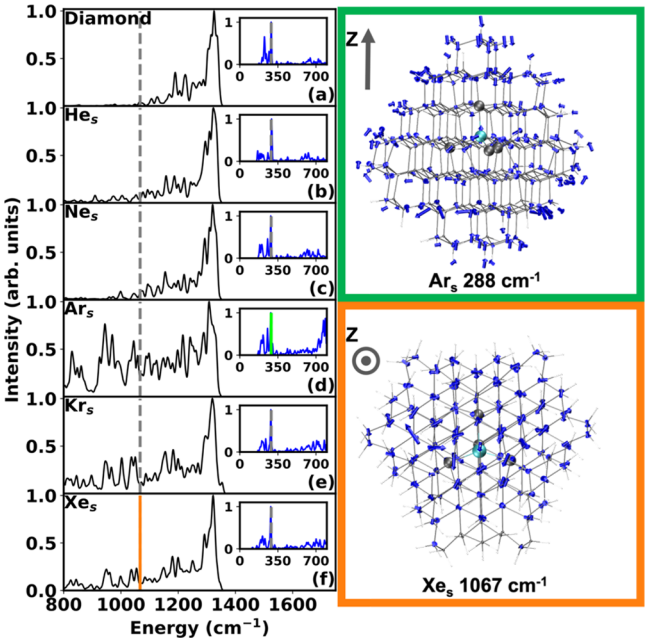

Figure 7. On the left are Raman vibrational spectra for the pure diamond (a) and (b–f) are the X_s-defect-containing diamond systems He, Ne, Ar, Kr, and Xe, respectively. From 800 to 1800 cm^{-1} are the spectra with artificially massed hydrogen to shift the hydrogen–carbon modes away from the carbon–carbon stretching modes. Inset into each plot are the Raman absorption spectra with regular massed hydrogen to show the low-energy responses. On the right are select normal modes with the noble gas in cyan, select carbon atoms in gray, the diamond lattice in wireframe, and the normal mode displacement vectors in dark blue. In gray is shown the orientation of the Cartesian Z axis, which aligns with the crystallographic ⟨111⟩ axis. Spectral locations of the select normal modes are color-labeled on the Raman spectra.

vacancy position, the second $\angle_{CXC}$ = 99.08° is between two carbons of two different vacancy positions, and the final $\angle_{CXC}$ = 180.0° is for two carbons on opposite sides of the dopant in two vacancy positions. Geometry optimization results in bond elongation because of the missing covalent bonds. The D_{3d} symmetry is mostly maintained except for the smallest dopant, He. The He atom forms a geometry similar to the nitrogen vacancy where the He occupies a carbon vacancy position. Thus, the geometric distortion is largest for the He dopant and lowers the local symmetry to C_{3v} from the split-vacancy structure.

3.2. Formation Enthalpy

To calculate the formation enthalpy for each noble gas system, we consider the following reaction:

$$X + C_{182}H_{142} \rightarrow XC_{182-n}H_{142} + nC \quad (1)$$

where X represents the noble gas atom in the system, n is an integer number for the quantity of carbon atoms that are removed from the system, and $C_{182}H_{142}$ and $XC_{182-n}H_{142}$ are the pure and defect-containing nanodiamond, respectively, with a H-passivated surface. The formation enthalpy $\Delta_f H$ of this reaction is calculated as

$$\Delta_f H(XC_{182-n}H_{142}) = H(XC_{182-n}H_{142}) - H(C_{182}H_{142}) - n\mu_C + \mu_X \quad (2)$$

Here, H is the enthalpy of the system. μ_C and μ_X are the chemical potentials for the carbon and noble gas, respectively. Chemical potentials were obtained through DFT calculations, as detailed in the Supporting Information.

As shown in Table 1, in general, the formation enthalpy of noble gas defects increases with the radius of the atom for all structures considered here. The same trend also has been reported in noble-gas-defected bulk diamond in earlier studies.[29] For all noble gas defects, except Xe, the trend is $\Delta H(X_i) < \Delta H(X_s) < \Delta H(X_iV)$. For Xe, the X_s structure is determined to have the lowest formation enthalpy.

While the magnitude of the formation enthalpy increases, the difference between the various defect configurations becomes smaller (see Figure 5) as the size of the noble gas atom increases. This is mainly due to destabilization of the X_i structure as the repulsion between the noble gas atom and nearby carbon atoms increases. The change in formation enthalpy for the vacancy-containing structures (X_iV) is smaller than the interstitial structure for all systems. This results in Xe having the lowest energetic differences between the possible defect structures.

3.3. Vibrational Signatures

Figures 6–8 show the computed Raman absorption spectra of noble-gas-doped nanodiamonds. Heavy hydrogens[17,40,77,78] (100 amu) are used to remove surface-capping C–H bond vibrations from the C–C vibrational region so we can analyze the vibrational signatures of the defects. In each plot, the

https://doi.org/10.1021/acsphyschemau.2c00072
ACS Phys. Chem Au 2023, 3, 299–310

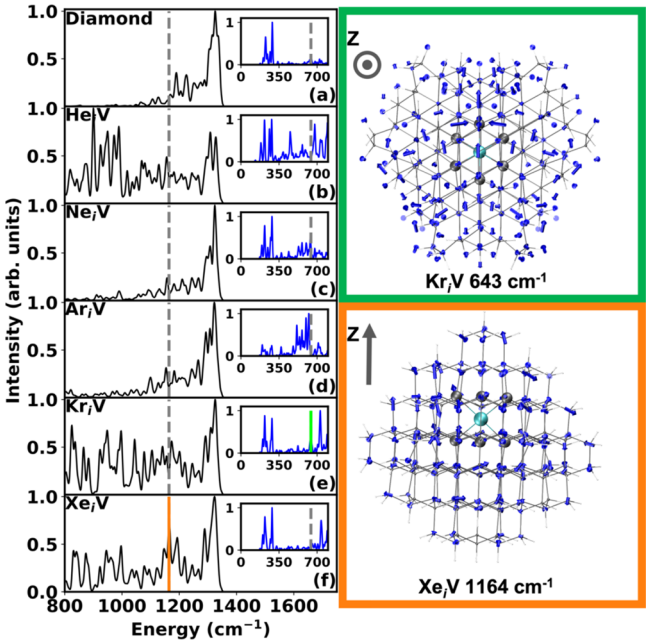

Figure 8. On the left are Raman vibrational spectra for the pure diamond (a), and (b–f) are the X_iV-defect-containing diamond systems He, Ne, Ar, Kr, and Xe, respectively. From 800 to 1800 cm^{-1} are the spectra with artificially massed hydrogen to shift the hydrogen–carbon modes away from the carbon–carbon stretching modes. Inset into each plot are the Raman absorption spectra with regular massed hydrogen to show the low-energy responses. On the right are select normal modes with the noble gas in cyan, select carbon atoms in gray, the diamond lattice in wireframe, and the normal mode displacement vectors in dark blue. In gray is shown the orientation of the Cartesian Z axis, which aligns with the crystallographic ⟨111⟩ axis. Spectral locations of the select normal modes are color-labeled on the Raman spectra.

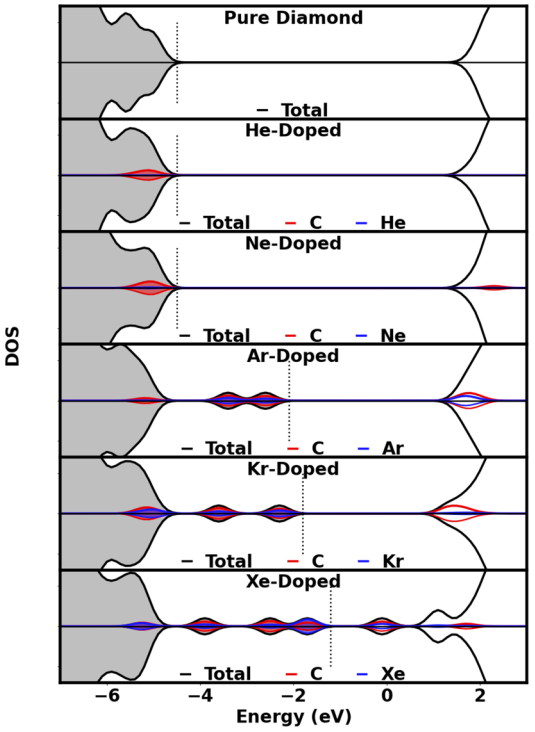

Figure 9. Partial density of states for the X_i noble gas systems. In each plot, the total density of states is shown (in black) with the contributions by the noble gas (in blue, 3×) and the carbons immediately surrounding the gas (in red) at the band gap. Positive and negative values correspond to spin-up and spin-down electrons, respectively. The spin-up and spin-down densities are the same for each plot since the systems are closed-shell. The top of the valence band is marked with a dotted, vertical line.

diamond Raman band at ∼1320 cm^{-1} can be observed, which indicates that the diamond lattice is maintained. A more in-depth examination of the responses belonging to pure nanodiamond can be found in ref 40.

Upon examination of the X_i vibrational spectra (Figure 6), it is observed that as the size of the noble gas dopant increases, the number of active Raman modes increases. This corresponds to a lowering of the symmetry, as marked in Figure 2, which corresponds to the noble gas moving from the high-symmetry interstitial point in the diamond. Examination of the diamond Raman peak indicates that as the size of the doped noble gas increases, additional peaks separate at higher energies (>∼ 1330 cm^{-1}). These peaks correspond to sp- and sp^2-like C–C bond vibrations caused by the noble gas expanding the doping site. This expansion causes compression to the rest of the diamond lattice. Similar absorption features have been seen in response to graphitic-like structures manifesting on the nanodiamond surface.[40,79−81]

The vibrational spectra for the X_s and X_iV geometries (Figures 7 and 8, respectively) show that the defects do not strongly affect the diamond vibrational band in the >1330 cm^{-1} range. The X_s and X_iV geometries show an increase in activity in the ∼800 to ∼1200 cm^{-1} energy region. These responses arise because of diamond lattice modes coupling to the vibrational modes of the defect center. The X_i defects (Ar–Xe) can be seen to also contain these modes because of the distorted diamond lattice around the noble gas defect.

The complex nature of the Raman spectra makes it challenging to differentiate between the different noble gases and their geometries. However, examination of these spectra is able to give interesting insights into the lattice deformations resulting from the presence of noble gas dopants.

3.4. Electronic Structure

In order to differentiate between the noble gas species, as well as the different geometries, the electronic structure is examined. Partial density of states (DOS) and predicted UV/vis absorption spectra are plotted in Figures 9–14. DOS plots have total density for both spin-up (positive values) and spin-down (negative values), as well as contributions by both the noble gas atom and surrounding nearest-neighbor carbon atoms, for intraband states plotted. The absorption spectra for each species contain the natural transition orbital (NTO) for the first, bright transition with the leaving, “hole,” orbital on the left and the arriving, “electron,” orbital on the right. In each figure, the first plot is the pure diamond for comparison. Because of quantum confinement effects, the band gap for the pure 1.4 nm diameter diamond is larger than the 5.5 eV bulk at ∼6.4 eV.[15,82] For hydrogen-terminated carbon clusters, quantum confinement is mostly mediated by the valence band.[15,83−85] Although additional virtual orbitals arising from surface hydrogens exist, they do not mix with localized defect states.[84,86]

Figure 9 contains the DOS for the X_i systems, which are the most stable configuration for all noble gas species except Xe. Although He and Ne color centers have been observed

https://doi.org/10.1021/acsphyschemau.2c00072
ACS Phys. Chem Au 2023, 3, 299–310

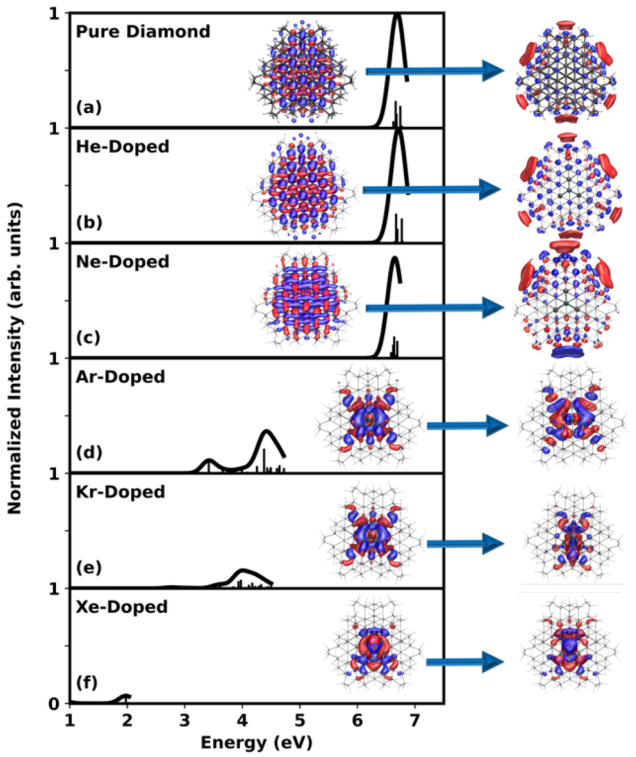

Figure 10. Absorption spectra for the X_i-doped diamond systems. The pure diamond system (a) is given as a point of reference, with the He, Ne, Ar, and Xe systems (b–f) showing the anticipated absorption features for each system. A Gaussian broadening of 0.12 eV has been applied to each LR-TDDFT response, given as black sticks, to form the spectra. The inset of each spectrum shows the leaving and arriving natural transition orbitals for the first, bright transition, which can be viewed in greater detail in the Supporting Information (Figures S1–S6). Table 2 contains absorption information for all geometric systems considered in this work.

experimentally[13,28] in bulk diamond, we did not observe any midgap states for the He_i or Ne_i configuration of the diamonds, which agrees with previous reports.[29] With similar atomic sizes, He and Ne X_i defects bring similar distortion to the nanodiamond lattice. This distortion, however, does not greatly affect the band gap of the doped systems, as can be seen in Figure 9. In addition, no He or Ne contributions are observed within the diamond band since neither He or Ne are able to bond to the surrounding carbons. Therefore, the lowest energy excited states of He and Ne X_i are interband transitions, which are similar to pure diamond transitions, at ∼6 eV. This is confirmed by the TDDFT results in Figure 10a–c, where both the absorption spectra and the leaving and arriving orbitals for the pure diamond and nanodiamonds with He and Ne dopants are of the same character. The energetic values for each transition are given in Table 2 and are shown to be similar.

For larger noble gas atoms in the interstitial position, lattice deformations and hybridization between the noble gas and carbon atoms give rise to midgap states. These midgap states allow for transitions lower in energy than the pure diamond band-to-band transitions at 6.43 eV. As shown in Table 2, the Kr X_i optical response is ∼0.6 eV lower in excitation energy than the Ar_i response (2.78 and 3.48 eV, respectively) and should be more detectable when probed by visible light. The

Table 2. First Bright ($f > 0.001$), Excited State for Each Geometry Considered, with Transition Symmetry Determined through Examination of the Natural Transition Orbitals for Each Excitation, as Considered within the C_s Geometry of the Overall Optimized Diamond Systems[a]

system	energy [eV] (oscillator strength)	transition
pure diamond	6.43 (0.0012)	band → band
He_{X_i}	6.44 (0.0012)	band → band
He_{X_s}	2.30 (0.0066)	a′ → a′
He_{X_iV}	1.02 (0.0276)	a″ → a′′
Ne_{X_i}	6.58 (0.0212)	band → band
Ne_{X_s}	2.16 (0.0068)	a″ → a′
Ne_{X_iV}	2.04 (0.0031)	a″ → a′
Ar_{X_i}	3.41 (0.0530)	a′ → a″
Ar_{X_s}	0.19 (0.0013)	a″ → a′
Ar_{X_iV}	2.46 (0.0028)	a′ → a′
Kr_{X_i}	2.78 (0.0044)	a′ → a′
Kr_{X_s}	0.79 (0.0116)	a′ → a′
Kr_{X_iV}	2.27 (0.0095)	a′ → a″
Xe_{X_i}	0.90 (0.0090)	a′ → a′
Xe_{X_s}	1.35 (0.0178)	a′ → a′
Xe_{X_iV}	2.20 (0.0309)	a′ → a″

[a]The absorption spectra for each geometry are plotted in Figures 10, 12, and 14 and contain the NTOs of the identified transition, which can also be located in the Supporting Information (Figures S1–S16).

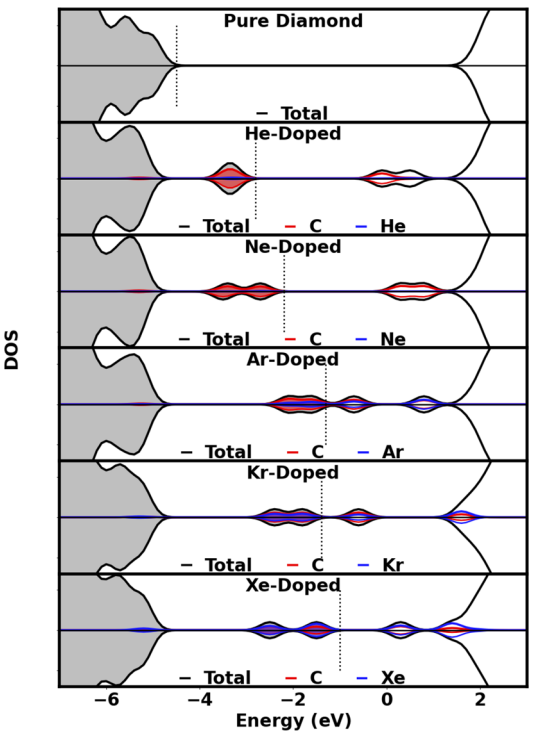

Figure 11. Partial density of states for the X_s noble gas systems. In each plot, the total density of states is shown (in black) with the contributions by the noble gas (in blue, 3×) and the carbons immediately surrounding the gas (in red) at the band gap. Positive and negative values correspond to spin-up and spin-down electrons, respectively. The top of the valence band is marked with a dotted, vertical line.

https://doi.org/10.1021/acsphyschemau.2c00072
ACS Phys. Chem Au 2023, 3, 299–310

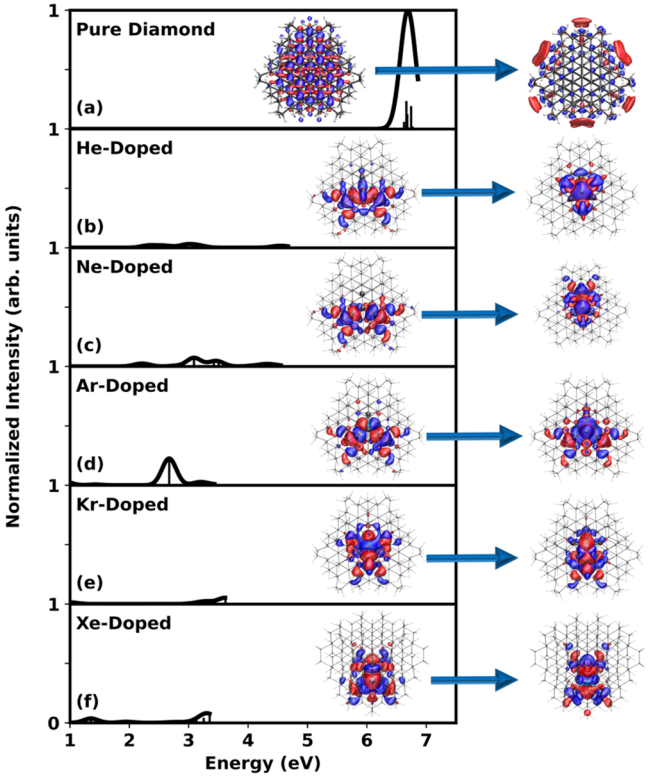

Figure 12. Absorption spectra for the X_s-doped diamond systems. The pure diamond system (a) is given as a point of reference, with the He, Ne, Ar, and Xe systems (b–f) showing the anticipated absorption features for each system. A Gaussian broadening of 0.12 eV has been applied to each LR-TDDFT response, given as black sticks, to form the spectra. The inset of each spectrum shows the leaving and arriving natural transition orbitals for the first, bright transition, which can be viewed in greater detail in the Supporting Information (Figures S1 and S7–S11). Table 2 contains absorption information for all geometric systems considered in this work.

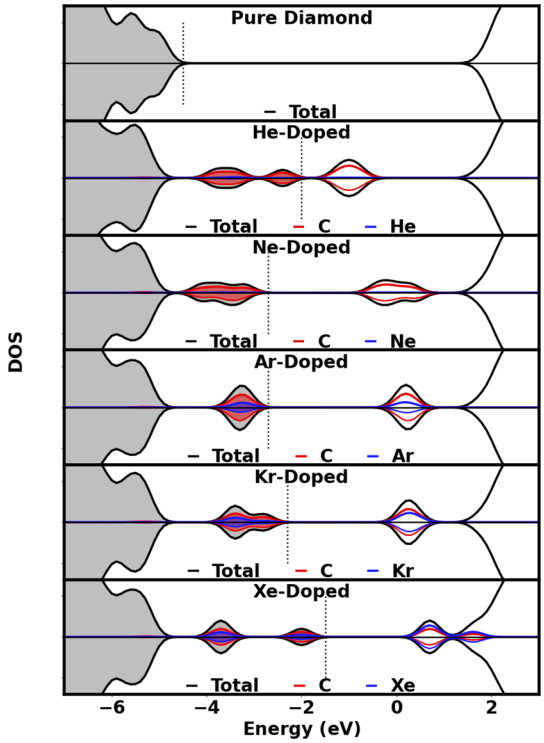

Figure 13. Partial density of states for the X_iV noble gas systems. In each plot, the total density of states is shown (in black) with the contributions by the noble gas (in blue, 3×) and the carbons immediately surrounding the gas (in red) at the band gap. Positive and negative values correspond to spin-up and spin-down electrons, respectively. The top of the valence band is marked with a dotted, vertical line.

NTOs inset into Figure 10 show these transitions to be localized around the noble gas dopant.

Examination of Figures 11 and 12 for the substitutional (X_s) systems demonstrate that all of the noble gas systems are able to introduce midgap states. In the case of the small dopants (He and Ne), this is surprising because neither were able to form color centers in the X_i systems. Examination of the DOS plot, however, shows that there are no contributions to the midgap states by the noble gas. This implies that instead of the noble gas being responsible for the midgap states, it is the carbon vacancy that is responsible, and the noble gas is inactive within the defect. While the leaving orbital for Ar_s looks similar to both the He and Ne X_s systems, and there is little contribution to the HOMO by Ar, the arriving orbitals can be seen to have Ar character. Since both Kr and Xe X_s systems have noble gas contributions to the midgap states, Ar is the smallest noble gas that is able to participate in the electronic transition, similar to what was observed for the X_i systems. This is seen again in Figures 13 and 14 for the divacancy systems. Molecular orbital diagrams for the most stable configuration for each noble gas dopant can be found in the Supporting Information (Figures S17–S23).

As shown in Table 2, the diamond systems containing Kr and Xe have absorption features within the visible energy range. Of particular interest is the Xe_iV system, which has two degenerate transitions at 2.20 eV originating from the highest occupied molecular orbital to the two degenerate molecular orbitals (Figure 14f). These transitions echo previous literature that has examined the Xe color center in diamond.[31] However, in our case, these responses have been blue-shifted from their value of 1.53 eV because of quantum confinement effects, similar to what has been seen before for nanodiamond systems.[18] While not predicted to be the ground state, the small difference in formation energy for the Xe center between different configurations in relation to the energy required to form the defect means that multiple geometries are expected to be able to form. Since the ZPL energy of Xe is comparable to the other widely studied nanodiamond defects, such as Si, Xe defects have high potential for spintronic applications where the heavier center can lead to longer coherence times.[87]

The TDDFT results, in combination with the formation energy results, explain why an Ar color center in diamond is challenging to observe experimentally. As shown in Figures 11 and 13, Ar_s, and Ar_iV are able to introduce midgap states that fall within the visible energy range (shown in Table 2). However, the large formation energy difference between the Ar_i system and both the Ar_s and Ar_iV systems make Ar_s and Ar_iV less common in diamond than Ar X_i defects, which do not have unfilled midgap states, as shown in Figure 9. When comparing the TDDFT-generated absorption spectrum for the most stable configuration for Ar and Xe in Figures 10 and 14, we can clearly see that the Xe system has responses in the visible range that the Ar system lacks.

These results indicate that noble gas centers in diamond are able to give rise to intraband states, which manifest as UV/vis

https://doi.org/10.1021/acsphyschemau.2c00072
ACS Phys. Chem Au 2023, 3, 299–310

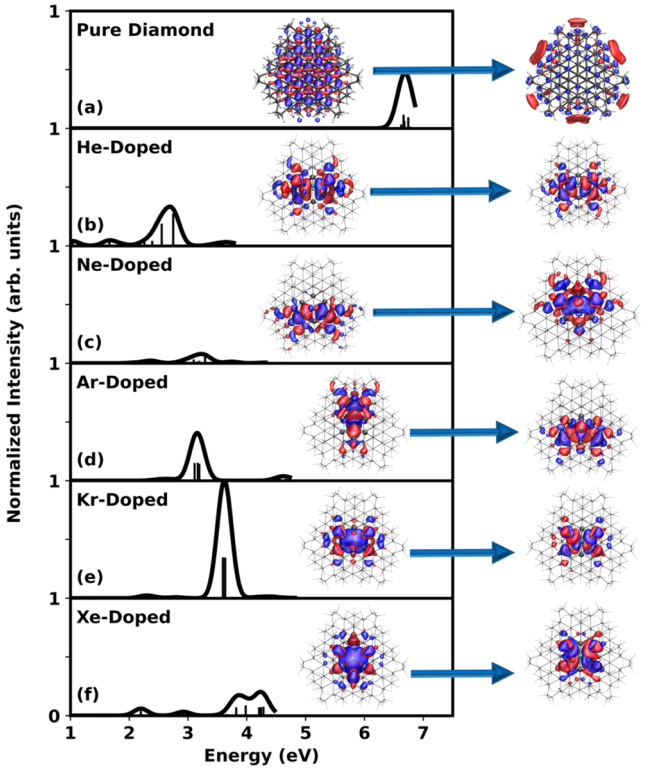

Figure 14. Absorption spectra for the X_iV-doped diamond systems. The pure diamond system (a) is given as a point of reference, with the He, Ne, Ar, and Xe systems (b–f) showing the anticipated absorption features for each system. A Gaussian broadening of 0.12 eV has been applied to each LR-TDDFT response, given as black sticks, to form the spectra. The inset of each spectrum shows the leaving and arriving natural transition orbitals for the first, bright transition, which can be viewed in greater detail in the Supporting Information (Figures S1 and S12–S16). Table 2 contains absorption information for all geometric systems considered in this work.

features. However, the required lattice deformations to introduce these states mean that, for noble gas systems smaller than Xe or Kr, it is highly unlikely to be experimentally realized.

4. CONCLUSION

In this work, noble gas (He, Ne, Ar, Kr, and Xe) defects in nanodiamond have been systematically studied using DFT. Several possible geometric configurations of each noble gas atom have been studied. The optical and Raman vibrational absorption spectra for each noble gas species have been constructed and examined. For the noble gas atoms, except Xe, the interstitial (X_i) geometry is the most stable configuration. It was determined that the formation energy difference between the X_i configuration and other configurations decreases with increasing atomic size. As such, for larger noble gas defects, it may be possible to form multiple geometric configurations. DOS results and absorption spectra unveil that Xe near-infrared range transitions are associated with a split-divacancy. Even though the Ar X_iV geometry introduces similar midgap states and allows bright midgap transitions, which should enable Ar as a potential color center, the formation energy of the defect is much higher than other Ar-containing geometric configurations. This explains why experimental UV–vis results have not found Ar color centers in diamond or nanodiamond, even though Ar has been experimentally incorporated within nanodiamond.[88] However, given that Kr shows absorption features within the visible energetic range (2.78 eV) for the most stable structure, it is possible that using Kr as a high-pressure–high-temperature pressure medium may lead to the formation of color centers.

ASSOCIATED CONTENT

Supporting Information

The Supporting Information is available free of charge at https://pubs.acs.org/doi/10.1021/acsphyschemau.2c00072.

Basis set comparison, formation enthalpy calculations, natural transition orbital images for the first bright transitions, and MO diagrams for the most stable geometric configurations (PDF)

AUTHOR INFORMATION

Corresponding Author

Xiaosong Li − *Department of Chemistry, University of Washington, Seattle, Washington 98195, United States;* orcid.org/0000-0001-7341-6240; Email: xsli@uw.edu

Authors

Ryan A. Beck − *Department of Chemistry, University of Washington, Seattle, Washington 98195, United States;* orcid.org/0000-0002-2953-970X

Yue Huang − *Department of Materials Science and Engineering, University of Washington, Seattle, Washington 98195, United States;* orcid.org/0000-0002-9927-1243

Alessio Petrone − *Dipartimento di Scienze Chimiche Angelo, I-80126 Napoli, Italy;* orcid.org/0000-0003-2232-9934

Joseph W. Abbott − *Laboratory of Computational Science and Modeling, Institute of Materials, École Polytechnique Fédérale de Lausanne, 1015 Lausanne, Switzerland;* orcid.org/0000-0002-0502-6790

Peter J. Pauzauskie − *Department of Materials Science and Engineering, University of Washington, Seattle, Washington 98195, United States;* orcid.org/0000-0002-1554-5949

Complete contact information is available at: https://pubs.acs.org/10.1021/acsphyschemau.2c00072

Author Contributions

‖These authors contributed equally to this work.

Notes

The authors declare no competing financial interest.

ACKNOWLEDGMENTS

The development of the computational spectroscopy method is supported by the NSF (CHE-2154346 to X.L.). The study of defects in nanodiamond is supported by the University of Washington Molecular Engineering Materials Center (DMR-1719797). A.P. is grateful for financial support from the Italian Ministry of University and Research (MUR) (Project AIM1829571-1 CUP E61G19000090002). This work was facilitated though the use of advanced computational, storage, and networking infrastructure provided by the Hyak supercomputer system and funded by the STF at the University of Washington.

REFERENCES

(1) Portet, C.; Yushin, G.; Gogotsi, Y. Electrochemical Performance of Carbon Onions, Nanodiamonds, Carbon Black and Multiwalled Nanotubs in Electrical Double Layer Capacitors. *Carbon* **2007**, *45*, 2511−2518.

(2) Behler, K.; Stravato, A.; Mochalin, V.; Korneva, G.; Yushin, G.; Gogotsi, Y. Nanodiamond-Polymer Composite Fibers and Coatings. *ACS Nano* **2009**, *3*, 363−369.

(3) Mochalin, V.; Neitzel, I.; Etzold, B.; Peterson, A.; Palmese, G.; Gogotsi, Y. Covalent Incorporation of Aminated Nanodiamond into an Epoxy Polymer Network. *ACS Nano* **2011**, *5*, 7494−7502.

(4) Chang, Y.-R.; Lee, H.-Y.; Chen, K.; Chang, C.-C.; Tsai, D.-S.; Fu, C.-C.; Lim, T.-S.; Tzeng, Y.-K.; Fang, C.-Y.; Han, C.-C.; Chang, H.-C.; Fann, W. Mass Production and Dynamic Imaging of Fluorescent Nanodiamonds. *Nat. Nano.* **2008**, *3*, 284−288.

(5) Mc Guinness, L. P.; Yan, Y.; Stacey, A.; Simpson, D. A.; Hall, L. T.; Maclaurin, D.; Prawer, S.; Mulvaney, P.; Wrachtrup, J.; Caruso, F.; Scholten, R. E.; Hollenberg, L. C. L. Quantum Measurement and Orientation Tracking of Fluorescent Nanodiamonds Inside Living Cells. *Nat. Nano.* **2011**, *6*, 358−363.

(6) Jelezko, F.; Gaebel, T.; Popa, I.; Domhan, M.; Gruber, A.; Wrachtrup, J. Observation of Coherent Oscillation of a Single Nuclear Spin and Realization of a Two-Qubit Conditional Quantum Gate. *Phys. Rev. Lett.* **2004**, *93*, 130501.

(7) Alkahtani, M. H.; Alghannam, F.; Jiang, L.; Almethen, A.; Rampersaud, A. A.; Brick, R.; Gomes, C. L.; Scully, M. O.; Hemmer, P. R. Fluorescent Nanodiamonds: Past, Present, and Future. *Nanophotonics* **2018**, *7*, 1423−1453.

(8) Holt, K. B. Diamond at the Nanoscale: Applications of Diamond Nanoparticles from Cellular Biomarkers to Quantum Computing. *Philos. Trans. R. Soc. A* **2007**, *365*, 2845−2861.

(9) Balasubramanian, G.; Chan, I. Y.; Kolesov, R.; Al-Hmoud, M.; Tisler, J.; Shin, C.; Kim, C.; Wojcik, A.; Hemmer, P. R.; Krueger, A.; Hanke, T.; Leitenstorfer, A.; Bratschitsch, R.; Jelezko, F.; Wrachtrup, J. Nanoscale Imaging Magnetometry with Diamond Spins Under Ambient Conditions. *Nature* **2008**, *455*, 648−651.

(10) Pauzauskie, P. J.; Crowhurst, J. C.; Worsley, M. A.; Laurence, T. A.; Kilcoyne, A. L. D.; Wang, Y.; Willey, T. M.; Visbeck, K. S.; Fakra, S. C.; Evans, W. J.; Zaug, J. M.; Satcher, J. H. Synthesis and Characterization of a Nanocrystalline Diamond Aerogel. *Proc. Natl. Acad. Sci. U.S.A.* **2011**, *108*, 8550−8553.

(11) Manandhar, S.; Roder, P. B.; Hanson, J. L.; Lim, M.; Smith, B. E.; Mann, A.; Pauzauskie, P. J. Rapid Sol−Gel Synthesis of Nanodiamond Aerogel. *J. Mater. Res.* **2014**, *29*, 2905−2911.

(12) Crane, M.; Petrone, A.; Beck, R. A.; Lim, M.; Zhou, X.; Li, X.; Stroud, R. M.; Pauzauskie, P. High Pressure, High Temperature Molecular Doping of Nanodiamond. *Sci. Adv.* **2019**, *5*, No. eaau6073.

(13) Zaitsev, A. M. Vibronic Spectra of Impurity-Related Optical Centers in Diamond. *Phys. Rev. B* **2000**, *61*, 12909.

(14) Ma, Y.; Rohlfing, M.; Gali, A. Excited States of the Negatively Charged Nitrogen-Vacancy Color Center in Diamond. *Phys. Rev. B* **2010**, *81*, 041204.

(15) Kaviani, M.; Deák, P.; Aradi, B.; Frauenheim, T.; Chou, J.-P.; Gali, A. Proper Surface Termination for Luminescent Near-Surface NV Centers in Diamond. *Nano Lett.* **2014**, *14*, 4772−4777.

(16) Petrone, A.; Goings, J. J.; Li, X. Quantum Confinement Effects on Optical Transitions in Nanodiamonds Containing Nitrogen Vacancies. *Phys. Rev. B* **2016**, *94*, 165402.

(17) Beck, R. A.; Lu, L.; Petrone, A.; Ong, A. C.; Pauzauskie, P. J.; Li, X. Spectroscopic Signatures of the B and H4 Polyatomic Nitrogen Aggregates in Nanodiamond. *J. Phys. Chem. C* **2020**, *124*, 18275−18283.

(18) Petrone, A.; Beck, R. A.; Kasper, J. M.; Li, X.; Huang, Y.; Crane, M.; Pauzauskie, P. Electronic Structures and Spectroscopic Signatures of Silicon-Vacancy Containing Nanodiamonds. *Phys. Rev. B* **2018**, *98*, 205405.

(19) Thiering, G.; Gali, A. Ab Initio Magneto-Optical Spectrum of Group-IV Vacancy Color Centers in Diamond. *Phys. Rev. X* **2018**, *8*, 021063.

(20) Burgess, R.; Johnson, L. H.; Mattey, D. P.; Harris, J. W.; Turner, G. He Ar and C Isotopes in Coated and Polycrystalline Diamonds. *Chem. Geol.* **1998**, *146*, 205−217.

(21) Burgess, R.; Layzelle, E.; Turner, G.; Harris, J. W. Constraints on the Age and Halogen Composition of Mantle Fluids in Siberian Coated Diamonds. *Earth Planet. Sci. Lett.* **2002**, *197*, 193−203.

(22) Lewis, R. S.; Ming, T.; Wacker, J. F.; Anders, E.; Steel, E. Interstellar Diamonds in Meteorites. *Nature* **1987**, *326*, 160−162.

(23) Ming, T.; Anders, E. Isotopic Anomalies of Ne, Xe, and C in Meteorites. II. Intersteller Diamond and SiC: Carriers of Exotic Noble Gasses. *Geochim. Cosmochim. Acta* **1988**, *52*, 1235−1244.

(24) Huss, G. R.; Ott, U.; Koscheev, A. P. Noble Gases in Presolar Diamonds III: Implications of Ion Implantation Experiments with Synthetic Nanodiamonds. *Meteorit. Planet. Sci.* **2008**, *43*, 1811−1826.

(25) Orwa, J. O.; Nugent, K. W.; Jamieson, D. N.; Prawer, S. Raman Investigation of Damage Caused by Deep Ion Implantation in Diamond. *Phys. Rev. B* **2000**, *62*, 5461.

(26) Prins, J. F. Graphitization and Related Variable-Range-Hopping Conduction in Ion-Implanted Diamond. *J. Phys. D* **2001**, *34*, 2089.

(27) Tkachev, V. D.; Zaitsev, A. M.; Tkachev, V. V. Chemical Activity of Noble Gases in Diamond. *Phys. Status Solidi B* **1985**, *129*, 129−133.

(28) Prestopino, G.; Marinelli, M.; Milani, E.; Verona, C.; Verona-Rinati, G.; Traina, P.; Moreva, E.; Degiovanni, I. P.; Genovese, M.; Ditalia Tchernij, S.; Picollo, F.; Olivero, P.; Forneris, J. Photo-physical Properties of He-Related Color Centers in Diamond. *Appl. Phys. Lett.* **2017**, *111*, 111105.

(29) Goss, J. P.; Eyre, R. J.; Briddon, P. R.; Mainwood, A. Density Functional Simulations of Noble-Gas Impurities in Diamond. *Phys. Rev. B* **2009**, *80*, 085204.

(30) Bergman, A. A.; Zaitsev, A. M.; Gorokhovsky, A. A. Polarization of Luminescence and Site Symmetry of the Xe Center in Diamond. *J. Lumin.* **2007**, *125*, 92−96.

(31) Sandstrom, R.; Ke, L.; Martin, A.; Wang, Z.; Kianinia, M.; Green, B.; Gao, W.; Aharonovich, I. Optical Properties of Implanted Xe Color Centers in Diamond. *Opt. Commun.* **2018**, *411*, 182−186.

(32) Drumm, D. W.; Per, M. C.; Russo, S. P.; Hollenberg, L. C. L. Thermodynamic Stability of Neutral Xe Defects in Diamond. *Phys. Rev. B* **2010**, *82*, 054102.

(33) Zaitsev, A. M.; Bergman, A. A.; Gorokhovsky, A. A.; Huang, M. Diamond Light Emitting Diode Activated with Xe Optical Centers. *Phys. Status Solidi A* **2006**, *203*, 638−642.

(34) Shiryaev, A. A.; Hinks, J. A.; Marks, N. A.; Greaves, G.; Valencia, F. J.; Donnelly, S. E.; González, R. I.; Kiwi, M.; Trigub, A. L.; Bringa, E. M.; Fogg, J. L.; Vlasov, I. I. Ion Implantation in Nanodiamonds: Size Effect and Energy Dependence. *Sci. Rep.* **2018**, *8*, 5099.

(35) Koscheev, A. P.; Gromov, M. D.; Mohapatra, R. K.; Ott, U. History of Trace Gases in Presolar Diamonds Inferred from Ion-Implantation Experiments. *Nature* **2001**, *412*, 615−617.

(36) Levinshteĭn, M. E.; Rumyantsev, S. L.; Shur, M. *Handbook Series on Semiconductor Parameters: Si, Ge, C (Diamond), GaAs, GaP, GaSb, InAs, InP, InSb*; World Scientific Publishing: Singapore, 1996; pp 58−76.

(37) Greiner, N. R.; Phillips, D. S.; Johnson, J. D.; Volk, F. Diamonds in Detonation Soot. *Nature* **1988**, *333*, 440−442.

(38) Dolmatov, V. Y. Detonation-Synthesis Nanodiamonds: Synthesis, Structure, Properties and Applications. *Russ. Chem. Rev.* **2007**, *76*, 339−360.

(39) Ōsawa, E. Monodisperse Single Nanodiamond Particulates. *Pure Appl. Chem.* **2008**, *80*, 1365−1379.

(40) Beck, R.; Petrone, A.; Kasper, J. M.; Crane, M. J.; Pauzauskie, P. J.; Li, X. Effect of Surface Passivation on Nanodiamond Crystallinity. *J. Phys. Chem. C* **2018**, *122*, 8573−8580.

(41) Takahashi, K.; Yoshikawa, A.; Sandhu, A. *Wide Bandgap Semiconductors: Fundamental Properties and Modern Photonic and Electronic Devices*; Springer: New York, NY, 2007; pp 97−230.

(42) Frisch, M. J.; Trucks, G. W.; Schlegel, H. B.; Scuseria, G. E.; Robb, M. A.; Cheeseman, J. R.; Scalmani, G.; Barone, V.; Petersson,

https://doi.org/10.1021/acsphyschemau.2c00072
ACS Phys. Chem Au 2023, 3, 299−310

G. A.; Nakatsuji, H.; Li, X.; Caricato, M.; Marenich, A. V.; Bloino, J.; Janesko, B. G.; Gomperts, R.; Mennucci, B.; Hratchian, H. P.; Ortiz, J. V.; Izmaylov, A. F.; Sonnenberg, J. L.; Williams-Young, D.; Ding, F.; Lipparini, F.; Egidi, F.; Goings, J.; Peng, B.; Petrone, A.; Henderson, T.; Ranasinghe, D.; Zakrzewski, V. G.; Gao, J.; Rega, N.; Zheng, G.; Liang, W.; Hada, M.; Ehara, M.; Toyota, K.; Fukuda, R.; Hasegawa, J.; Ishida, M.; Nakajima, T.; Honda, Y.; Kitao, O.; Nakai, H.; Vreven, T.; Throssell, K.; Montgomery, J. A., Jr.; Peralta, J. E.; Ogliaro, F.; Bearpark, M. J.; Heyd, J. J.; Brothers, E. N.; Kudin, K. N.; Staroverov, V. N.; Keith, T. A.; Kobayashi, R.; Normand, J.; Raghavachari, K.; Rendell, A. P.; Burant, J. C.; Iyengar, S. S.; Tomasi, J.; Cossi, M.; Millam, J. M.; Klene, M.; Adamo, C.; Cammi, R.; Ochterski, J. W.; Martin, R. L.; Morokuma, K.; Farkas, O.; Foresman, J. B.; Fox, D. J. *Gaussian 16*, Revision *A.03*; Gaussian Inc.: Wallingford CT, 2016.

(43) Becke, A. D. Density-Functional Thermochemistry. III. The Role of Exact Exchange. *J. Chem. Phys.* **1993**, *98*, 5648.

(44) Lee, C.; Yang, W.; Parr, R. G. Development of the Colle-Salvetti Correlation-Energy Formula into a Functional of the Electron Density. *Phys. Rev. B* **1988**, *37*, 785.

(45) Miehlich, B.; Savin, A.; Stoll, H.; Preuss, H. Results Obtained with the Correlation Energy Density Functionals of Becke and Lee, Yang and Parr. *Chem. Phys. Lett.* **1989**, *157*, 200−206.

(46) Jr, T. H. D.; Hay, P. J. *Methods of electronic structure theory*; Schaefer, H. F., Ed.; Modern Theoretical Chemistry, Vol. *3*; Springer: New York, NY, 1977; pp 1−27.

(47) Fuentealba, P.; Preuss, H.; Stoll, H.; von Szentpály, L. A Proper Account of Core-Polarization with Pseudopotentials - Single Valence-Electron Alkali Compounds. *Chem. Phys. Lett.* **1982**, *89*, 418−422.

(48) von Szentpály, L.; Fuentealba, P.; Preuss, H.; Stoll, H. Pseudopotential Calculations on Rb+2, Cs+2, RbH+, CsH+ and the Mixed Alkali Dimer Ions. *Chem. Phys. Lett.* **1982**, *93*, 555−559.

(49) Fuentealba, P.; Stoll, H.; von Szentpály, L.; Schwerdtfeger, P.; Preuss, H. On the Reliability of Semi-Emperical Pseudopotentials - Simulation of Hartree-Fock and Dirac-Fock Results. *J. Phys. B* **1983**, *16*, L323−L328.

(50) Stoll, H.; Fuentealba, P.; Schwerdtfeger, P.; Flad, J.; von Szentpály, L.; Preuss, H. Cu and Ag as One-Valence-Electron Atoms - CI Results and Quadrupole Corrections of Cu2, Ag2, CuH, and AgH. *J. Chem. Phys.* **1984**, *81*, 2732−2736.

(51) Fuentealba, P.; von Szentpály, L.; Preuss, H.; Stoll, H. Pseudopotential Calculations for Alkaline-Earth Atoms. *J. Phys. B* **1985**, *18*, 1287−1296.

(52) Wedig, U.; Dolg, M.; Preuss, H. *Quantum Chemistry: The Challenge of Transition Metals and Coordination Chemistry*; Springer, Dordrecht, 1986; pp 79−89.

(53) Dolg, M.; Wedig, U.; Stoll, H.; Preuss, H. Energy-Adjusted Ab Initio Pseudopotentials for the First Row Transition Elements. *J. Chem. Phys.* **1987**, *86*, 866−872.

(54) Igel-Mann, G.; Stoll, H.; Preuss, H. Pseudopotentials for main group elements (IIIa through VIIa). *Mol. Phys.* **1988**, *65*, 1321−1328.

(55) Dolg, M.; Stoll, H.; Preuss, H. Energy-Adjusted Ab Initio Pseudopotentials for the Rare Earch Elements. *J. Chem. Phys.* **1989**, *90*, 1730−1734.

(56) Schwerdtfeger, P.; Dolg, M.; Schwarz, W. H. E.; Bowmaker, G. A.; Boyd, P. D. W. Relativistic Effects in Gold Chemistry. 1. Diatomic Gold Compounds. *J. Chem. Phys.* **1989**, *91*, 1762−1774.

(57) Dolg, M.; Stoll, H.; Savin, A.; Preuss, H. Energy-Adjusted Pseudopotentials for the Rare-Earth Elements. *Theor. Chem. Acc.* **1989**, *75*, 173−194.

(58) Andrae, D.; Haeussermann, U.; Dolg, M.; Stoll, H.; Preuss, H. Energy- Adjusted Ab Initio Pseudopotentials for the 2nd and 3rd Row Transition-Elements. *Theor. Chem. Acc.* **1990**, *77*, 123−141.

(59) Dolg, M.; Fulde, P.; Kuchle, W.; Neumann, C.-S.; Stoll, H. Ground State Calculations of Di-pi-cyclooctatetraene Cerium. *J. Chem. Phys.* **1991**, *94*, 3011−3017.

(60) Kaupp, M.; v. R. Schleyer, P.; Stoll, H.; Preuss, H. Pseudopotential Approaches to CA, SR, and BA Hybrids. Why are Some Alkaline-Earch MX2 Compounds Bent? *J. Chem. Phys.* **1991**, *94*, 1360−1366.

(61) Kuechle, W.; Dolg, M.; Stoll, H.; Preuss, H. Ab Initio Pseudopotentials for HG through RN. 1. Parameter Sets and Atomic Calculations. *Mol. Phys.* **1991**, *74*, 1245−1263.

(62) Dolg, M.; Stoll, H.; Flad, H.-J.; Preuss, H. Ab Initio Pseudopotential Study of Yb and YbO. *J. Chem. Phys.* **1992**, *97*, 1162−1173.

(63) Bergner, A.; Dolg, M.; Kuechle, W.; Stoll, H.; Preuss, H. Ab Initio Energy-Adjusted Pseudopotentials for Elements of Gruops 13−17. *Mol. Phys.* **1993**, *80*, 1431−1441.

(64) Dolg, M.; Stoll, H.; Preuss, H. A Combination of Quasi-Relativistic Pseudopotential and Ligand-Field Calculations for Lanthanoid Compounds. *Theor. Chem. Acc.* **1993**, *85*, 441−450.

(65) Haussermann, U.; Dolg, M.; Stoll, H.; Preuss, H.; Schwerdtfeger, P.; Pitzer, R.M. Accuracy of Energy-Adjusted Quasi-Relativistic Ab Initio Pseudopotentials - All-Electron and Pseudopotential Benchmark Calculations for HG, HGH and their Cations. *Mol. Phys.* **1993**, *78*, 1211−1224.

(66) Dolg, M.; Stoll, H.; Preuss, H.; Pitzer, R. M. Relativistic and Correlation-Effects for element 105 (Hahnium, Ha) - A Comparative-Study of M and MO (M = NB,TA,HA) Using Energy-Adjusted Ab Initio Pseudopotentials. *J. Phys. Chem.* **1993**, *97*, 5852−5859.

(67) Kuechle, W.; Dolg, M.; Stoll, H.; Preuss, H. Energy-Adjusted Pseudopotentials for the Actinides. Parameter Sets and Test Calculations for Thorium and Thorium Molecules. *J. Chem. Phys.* **1994**, *100*, 7535−7542.

(68) Nicklass, A.; Dolg, M.; Stoll, H.; Preuss, H. Ab Initio Energy-Adjusted Pseudopotentials for the Noble Gases Ne through Xe: Calculation of Atomic Dipole and Quadrupole Polarizabilities. *J. Chem. Phys.* **1995**, *102*, 8942.

(69) Leininger, T.; Nicklass, A.; Stoll, H.; Dolg, M.; Schwerdtfeger, P. The Accuracy of the Pseudopotential Approximation. II. A Comparison of Various Core Sizes for Indium Pseudopotentials in Calculations for Spectroscopic Constants of InH, InF, and InCl. *J. Chem. Phys.* **1996**, *105*, 1052−1059.

(70) Cao, X. Y.; Dolg, M. Valence Basis Sets for Relativistic Energy-Consistent Small-Core Lanthanide Pseudopotentials. *J. Chem. Phys.* **2001**, *115*, 7348−7355.

(71) Cao, X. Y.; Dolg, M. Segmented Contraction Scheme for Small-Core Lanthanide Pseudopotential Basis Sets. *J. Mol. Struct.* **2002**, *581*, 139−147.

(72) Casida, M. E. Time-Dependent Density Functional Response Theory for Molecules. In *Recent Advances in Density Functional Methods: (Part I)*, Vol. *1*; Chong, D. P., Ed.; World Scientific Publishing: Singapore, 1995; pp 155−193.

(73) Dreuw, A.; Head-Gordon, M. Single-Reference Ab Initio Methods for the Calculation of Excited States of Large Molecules. *Chem. Rev.* **2005**, *105*, 4009−4037.

(74) Stratmann, R. E.; Scuseria, G. E.; Frisch, M. J. An Efficient Implementation of Time-Dependent Density-Functional Theory for the Calculation of Excitation Energies of Large Molecules. *J. Chem. Phys.* **1998**, *109*, 8218−8224.

(75) Liang, W.; Fischer, S. A.; Frisch, M. J.; Li, X. Energy-Specific Linear Response TDHF/TDDFT for Calculating High-Energy Excited States. *J. Chem. Theory Comput.h* **2011**, *7*, 3540−3547.

(76) Gali, A.; Maze, J. R. Ab Initio Study of the Split Silicon-Vacancy Defect in Diamond: Electronic Structure and Related Properties. *Phys. Rev. B* **2013**, *88*, 235205.

(77) Filik, J.; Harvey, J. N.; Allan, N.; May, P.; Dahl, J.; Liu, S.; Carlson, R. Raman Spectroscopy of Nanocrystalline Diamond: An Ab Initio Approach. *Phys. Rev. B* **2006**, *74*, 035423.

(78) Li, W.; Irle, S.; Witek, H. A. Convergence in the Evolution of Nanodiamond Raman Spectra with Particle Size: A Theoretical Investigation. *ACS Nano* **2010**, *4*, 4475−4486.

(79) Chang, S. L.; Dwyer, C.; Osawa, E.; Barnard, A. S. Size Dependent Surface Reconstruction in Detonation Nanodiamonds. *Nanoscale Horiz* **2018**, *3*, 213−217.

(80) Barnard, A. S.; Russo, S. P.; Snook, I. K. *Ab initio* Modeling of B and N in C_{29} and $C_{29}H_{24}$ Nanodiamond. *J. Chem. Phys.* **2003**, *118*, 10725−10728.

https://doi.org/10.1021/acsphyschemau.2c00072
ACS Phys. Chem Au 2023, 3, 299−310

(81) Galli, G. *Computer-Based Modeling of Novel Carbon Systems and Their Properties*; Springer Science+Business Media B.V.: Van Godewijckstraat, Netherlands, 2010; pp 37−56.
(82) Raty, J.-Y.; Galli, G.; Bostedt, C.; van Buuren, T. W.; Terminello, L. J. Quantum Confinement and Fullerenelike Surface Reconstructions in Nanodiamonds. *Phys. Rev. Lett.* **2003**, *90*, 037401.
(83) Vlasov, I. I.; Shiryaev, A. A.; Rendler, T.; Steinert, S.; Lee, S.-Y.; Antonov, D.; Vörös, M.; Jelezko, F.; Fisenko, A. V.; Semjonova, L. F.; Biskupek, J.; Kaiser, U.; Lebedev, O. I.; Sildos, I.; Hemmer, P. R.; Konov, V. I.; Gali, A.; Wrachtrup, J. Molecular-Sized Fluorescent Nanodiamonds. *Nat. Nano.* **2014**, *9*, 54−58.
(84) Ekimov, E. A.; Kondrin, M. V. Influence of Confinement and Surface Functionalization Effects on Fluorescent Properties of the Impurity-Vacancy Complexes in Ultrasmall Nanodiamonds. *Physica B* **2022**, *647*, 414369.
(85) Vörös, M.; Gali, A. Optical Absorption of Diamond Nanocrystals from Ab Initio Density-Functional Calculations. *Phys. Rev. B* **2009**, *80*, No. 161411(R).
(86) Lin, C.-K.; Wang, Y.-H.; Chang, H.-C.; Hayashi, M.; Lin, S. H. One-and Two-Photon Absorption Properties of Diamond Nitrogen-Vacancy Defect Centers: A Theoretical Study. *J. Chem. Phys.* **2008**, *129*, 124714.
(87) Defo, R. K.; Kaxiras, E.; Richardson, S. L. How Carbon Vacancies can affect the Properties of Group IV Color Centers in Diamond: A Study of Thermodynamics and Kinetics. *J. Appl. Phys.* **2019**, *126*, 195103.
(88) Crane, M. J.; Smith, B. E.; Meisenheimer, P. B.; Zhou, X.; Stroud, R. M.; Davis, E. J.; Pauzauskie, P. J. Photothermal Effects During Nanodiamond Synthesis from a Carbon Aerogel in a Laser-Heated Diamond Anvil Cell. *Diam Relat Mater.* **2018**, *87*, 134−142.

https://doi.org/10.1021/acsphyschemau.2c00072
ACS Phys. Chem Au 2023, 3, 299−310